JOURNAL OF GEOPHYSICAL RESEARCH: SPACE PHYSICS, VOL. 118, 3700–3711, doi:10.1002/jgra.50358, 2013

Simulated kinetic effects of the corona and solar cycle on high altitude ion transport at Mars

S. M. Curry,[1] M. Liemohn,[1] X. Fang,[2] D. Brain,[2] and Y. Ma[3]

Received 31 January 2013; revised 22 May 2013; accepted 24 May 2013; published 17 June 2013.

[1] We present results from the Mars Test Particle (MTP) simulation as part of a community-wide model comparison in order to quantify the role of different neutral atmospheric conditions in planetary ion transport and escape. This study examines the effects of individual ion motion by simulating particle trajectories for three cases: solar minimum without the neutral corona, solar minimum with the inclusion of the neutral corona, and solar maximum with the inclusion of the neutral corona. The MTP simulates 1.5 billion test particles through background electric and magnetic fields computed by a global magnetohydrodynamic model. By implementing virtual detectors in the simulation, the MTP has generated velocity space distributions of pickup ions and quantifies the ion acceleration at different spatial locations. The study found that the inclusion of a hot neutral corona greatly affects the total O^+ production and subsequent loss, roughly doubling the total escape for solar minimum conditions and directly contributing to high energy sources above 10 keV. The solar cycle influences the amount of O^+ flux observed by the virtual detectors, increasing the O^+ flux and total escape by an order of magnitude from solar minimum to maximum. Additionally, solar maximum case induces greater mass loading of the magnetic fields, which decreases the gyroradius of the ions and redirects a significant ion population downtail to subsequently escape.

Citation: Curry, S. M., M. Liemohn, X. Fang, D. Brain, and Y. Ma (2013), Simulated kinetic effects of the corona and solar cycle on high altitude ion transport at Mars, *J. Geophys. Res. Space Physics*, *118*, 3700–3711, doi:10.1002/jgra.50358.

1. Introduction

[2] Questions surrounding the role of oxygen escape in the evolution of CO_2 and H_2O inventories in Mars' atmosphere have motivated numerous studies on atmospheric loss, particularly with respect to nonthermal processes [*Jakosky and Phillips*, 2002]. In the absence of a global dipole magnetic field to shield Mars' atmosphere, pickup ions are created when planetary neutrals are ionized and subsequently accelerated and swept away by the solar wind convective electric field. Because Mars has an extended hot oxygen corona due to dissociative recombination [*Fox and Hac*, 1997; *Nagy et al.*, 2004; *Chaufray et al.*, 2007; *Cipriani et al.*, 2007; *Barabash and Holmstrom*, 2002; *Valeille et al.*, 2009], the escape of oxygen ions constitutes one of the dominant sources of nonthermal atmospheric loss [e.g., *Kallio et al.*, 2011, and references therein].

[3] In order to model the Mars solar wind interaction, the scientific community have generally used a magnetohydrodynamic (MHD) approach, a hybrid approach, or a test particle approach. The MHD models [*Liu et al.*, 1999; *Ma et al.*, 2004; *Harnett and Winglee*, 2006; *Jin et al.*, 2006; *Terada et al.*, 2009; *Najib et al.*, 2011] self-consistently solve fluid equations for the configuration of charged particles and magnetic fields around a planet. Hybrid models also self-consistently solve for the plasma parameters and fields and treat the plasma environment as a combination of individual ions and a massless neutralizing electron fluid [*Modolo et al.*, 2005; *Boesswetter et al.*, 2007; *Kallio et al.*, 2010; *Brecht and Ledvina*, 2010]. A third alternative for exploring the Mars plasma environment is a test particle simulation, which treats the ions as particles and follows their trajectories in a prescribed field configuration [e.g., *Luhmann and Kozyra*, 1991; *Cipriani et al.*, 2007; *Fang et al.*, 2008; *Andersson et al.*, 2010]. Although this approach lacks self-consistency because the test particles do not modify the background fields, it does allow the investigation of high resolution velocity space distributions (VSDs).

[4] *Brain et al.* [2010] conducted a global model comparison activity involving many of the current models for the Martian plasma interaction using a common set of input and boundary conditions for a nominal solar wind case. A number of diagnostics were extracted from the simulations and compared, including 1-D pressure profiles, 2-D slices of ion density, and global atmospheric escape rates. Among

[1]Department of Atmospheric and Space Sciences, University of Michigan, Ann Arbor, Michigan, USA.
[2]Laboratory for Atmospheric and Space Physics, University of Colorado Boulder, Boulder, Colorado, USA.
[3]Institute of Geophysics and Planetary Physics, University of California, Los Angeles, California, USA.

Corresponding author: S. M. Curry, Department of Atmospheric and Space Sciences, University of Michigan, 2455 Hayward Street, Space Research Building, Ann Arbor, MI 48109, USA. (smcurry@umich.edu)

2169-9380/13/10.1002/jgra.50358

these diagnostics, *Brain et al.* [2010] noted over an order of magnitude difference among the different models in the simulated O^+ escape rates for the selected input conditions.

[5] A follow-on study is underway using a common set of rate coefficients [*Brain et al.*, 2012], neutral atmospheric profiles and identical upstream conditions. As part of this global model comparison effort, multiple simulations were run for solar minimum and maximum conditions. This study investigates the influence of the oxygen corona and solar cycle on the individual ion trajectories. Using the MTP simulation to solve for these kinetic effects, the O^+ trajectories can be translated into virtual detections at different spatial locations around the planet. By examining different fluxes and energy ranges for the VSDs, we quantify the influence of the solar cycle and hot corona. The focus of this investigation is to use the MTP to explore how variations in the neutral atmosphere influence O^+ acceleration and loss.

2. Methods

2.1. Models

[6] Test particle simulations are not self-consistent in that they do not calculate the convective electric and magnetic fields and thus require input background fields. For this study, the 3-D, multispecies MHD model of *Ma et al.* [2004] provided the background fields that incorporated the established global model comparison inputs for three different cases.

[7] The *Ma et al.* [2004] study uses the BATS-R-US (Block Adaptive-Tree Solar wind Roe-type Upwind Scheme) MHD model to solve the dimensionless conservative form of the MHD equations for the plasma and field parameters in the plasma environment around Mars. The model uses a spherical grid structure that extends from the lower boundary in the ionosphere at 100 km to an outer boundary beyond the bow shock at 8 R_M upstream and 24 R_M downstream. The radial cell sizes are 10 km near the planet in order to capture the ionospheric profile and then exponentially increases with radial distance. The MHD model solves for separate solutions of the H^+, O^+, O_2^+, and CO_2^+ mass densities. The convective electric field is calculated by

$$\mathbf{E} = -\mathbf{U} \times \mathbf{B}$$

where **U** is the bulk flow velocity and **B** is the magnetic field; the Hall term is neglected for these simulations.

[8] The MTP simulation is a parallelized 3-D Monte Carlo model that follows the trajectory of individual ions (in this case O^+) along the background electric and magnetic field. This model is discussed in detail in *Curry et al.* [2013] and *Fang et al.* [2008]. The MTP simulation solves Newton's equation of motion for the pickup ions, where their transport is dictated by the Lorentz force. Ion production begins by launching the same number of particles per source cell, using a Maxwellian energy distribution of the neutral temperature and isotropic angular distribution. The MTP uses the Monte Carlo method to randomly assign the particles' initial position, energy, and direction. The total ion production in each cell is divided by the total number of test particles per unit time in order to weight each particle. The simulation tracks each particle until it hits the inner boundary at 300 km or the outer boundary at 3 R_M.

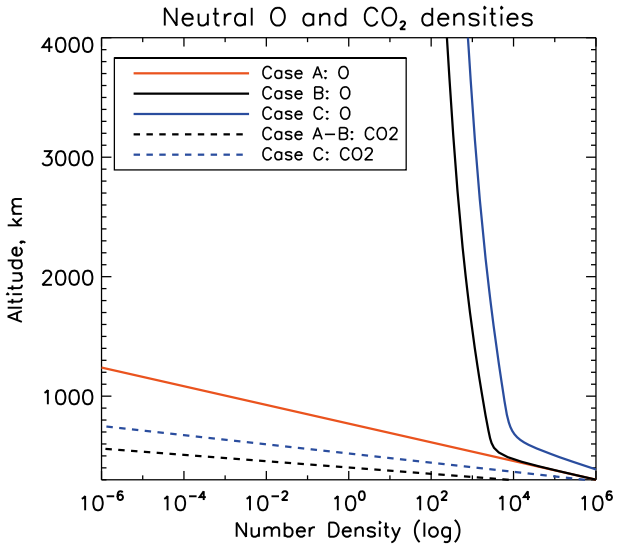

Figure 1. An altitude profile of the neutral atmosphere from 200 km to 3 R_M for Cases A, B, and C.

Due to the assumption that the model is collisionless, the inner boundary is placed well above the nominal exobase, 180–250 km, [*Fox*, 2009] for solar minimum and maximum cases. The simulation uses a spherical grid with cell resolution of 5° by 5° and grid spacing with respect to logarithmic radial distance [*Fang et al.*, 2008]. The MTP used over 1.5 billion test particles for this simulation, whose angular distribution, energy, and velocity are recorded at virtual detectors and constructed into velocity space distributions. The virtual detectors can be placed anywhere in the simulation in order to record the flux, position, and flight direction of the particles.

2.2. Neutral Atmosphere and Ion Production

[9] The global model comparison of *Brain et al.* [2012] uses three common input scenarios: Case A constitutes solar minimum conditions without a corona, Case B has solar minimum conditions with a corona, and Case C follows with solar maximum conditions including a corona. All cases exclude the Martian crustal fields. The solar wind is composed of protons with a density of 2.7 cm^{-3} with a temperature of 13 eV and electron temperature of 9 eV. The bulk velocity flows radially from the Sun at a speed of 485 km/s, and the interplanetary magnetic field (IMF) is consistent with a Parker spiral field of 3 nT configured at (–1.634, 2.516, and 0.0 nT) in the Mars Solar Orbital (MSO) coordinate system where $-X$ is in the direction of the bulk flow, $+Y$ is in the direction anti-parallel to Mars' orbital (instantaneous) velocity, and $+Z$ completes the right-hand system. Because we define the IMF where $B_X < 0$ and $B_Y > 0$, this is an "away sector" field in the ecliptic plane that points from dusk toward dawn at a 57° angle with respect to the $-X$ axis. The neutral atmosphere and corona are constructed from the simulated outputs of *Bougher et al.* [2004], *Chaufray et al.* [2007], & *Bougher et al.* [2008], and *Valeille et al.* [2010], seen in Figure 1. While a neutral hot hydrogen corona was included for Cases B and C, it is not plotted in Figure 1 because the MTP simulation discussed here does not trace H^+.

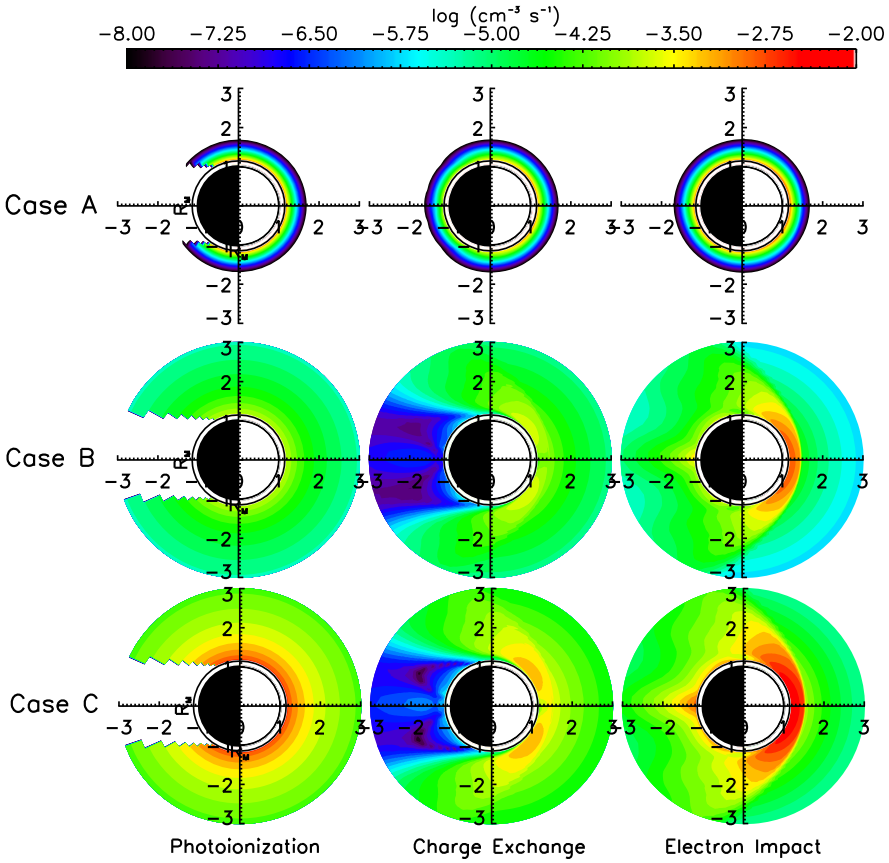

Figure 2. The equatorial view of the production rate for the three ion production mechanisms for each case from 300 km to 3 R_M.

[10] In this study, the MTP follows O^+ throughout the simulation, beginning with time-independent production in each cell. The total ion production is the product of the neutral oxygen density, the cell volume, and the reaction rate for each of the three production mechanisms: photoionization, charge exchange, and electron impact. For photoionization, instead of incorporating solar zenith angle dependence, an optical shadow directly behind the planet is used due the atmosphere being optically thin above 300 km [*Curry et al.*, 2013]. Constant photoionization rates of 8.89×10^{-8} and 2.73×10^{-7} s^{-1} are employed everywhere but in the optical shadow for solar minimum and maximum, respectively.

[11] For charge exchange, two reactions produce O^+. The first reaction is through $CO_2^+ + O \rightarrow CO_2 + O^+$, with a constant production rate of 9.6×10^{-11} cm^{-3} s^{-1}. The second charge exchange reaction is based on the collision of solar wind protons and atomic oxygen $H^+ + O \rightarrow H + O^+$. The reaction rate here (k_{ch}, cm^3/s) is proportional to the local bulk flow speed (v_{bulk}, cm/s) and the ionization cross section for H^+–O reaction (σ, cm^2), as seen in equation (1). As described above, the production rate for the second reaction is the product of the neutral oxygen density, the proton density, the cell volume, and the reaction rate (k_{ch}). Thus, the high altitude neutrals are ionized as a function of the bulk velocity of the hot solar wind protons (hot energetic charge exchange).

$$k_{ch} = v_{bulk} \times \sigma \quad (1)$$

[12] For electron impact, the reaction rate is based on the electron temperature. We have adopted values from the *Cravens et al.* [1987] study on electron impact ionization rates for several neutral species (including atomic oxygen) that can be fitted with a logarithmic polynomial function of the electron temperature. A more detailed discussion of ionization mechanisms can be found in *Curry et al.* [2013].

[13] Figure 2 illustrates the three ion production mechanisms for each case. The figure is an equatorial view of the production rate for each mechanism and for each case from the inner boundary of 300 km to the outer boundary of 3 R_M. The lack of a corona is clear in Case A, while the hot corona is ionized in Cases B and C. Due to the enhanced neutral atmosphere, the increase in production from solar minimum to maximum is relatively linear and symmetric. Because the solar wind conditions remain the same for all three cases, the neutral atmosphere and ion production are critical to examine when analyzing the trajectories and escape of O^+, which *Curry et al.* [2013] discuss in detail. In particular, high rates of ion production, often occurring inside the bow shock, can cause mass loading [*Bauske et al.*, 1998; *Shinagawa and Bougher*, 1999; *Lundin et al.*, 2011a]. This process occurs between a plasma in motion and a plasma at rest; at Mars, the planetary ions at rest are picked up by the solar wind and accelerated by the convective electric field. In order to preserve the conservation of momentum, the solar wind is decelerated by the increase in mass [*Dubinin et al.*, 2011]. This in turn can increase the magnetic field, which

subsequently affects the gyromotion of an individual particle (see equations 1–5 and Figures 5 and 9 from the *Ma et al.* [2004] study).

3. Results

[14] Here we present flux, energy, and velocity space distributions from the virtual detectors in order to highlight the influence of the corona and solar cycle on individual particle motion. The following results adopt a Cartesian coordinate system corresponding to the Mars Solar Orbital (MSO) coordinate system, where the system is centered at Mars, X_{MSO} points toward the sun, Y_{MSO} is aligned with the dusk direction in Mars' orbital plane, and Z_{MSO} points north to complete the right-hand system. For this study, the detectors were placed downtail (directly along the X_{MSO} line), and at the North and South Poles (directly along the Z_{MSO} line above and below the planet). They were radially spaced 0.2 R_M apart from 1.1–3.0 R_M (only a selection will be shown).

3.1. Influence of the Corona

[15] A comparison of the results from Cases A and B allows us to examine the influence of the hot oxygen corona on high altitude ion motion while a comparison of Cases B and C isolates the influence of the solar cycle. Beginning with an examination of the corona, Figure 3 shows the number flux at 1.1, 1.5, 2, and 2.5 R_M radially downtail from the planet where the number flux is plotted as a function of logarithmic energy.

[16] Cases A and B have very different energy-flux signatures, but follow a similar trend as the detector is moved further downtail. In each case, the peak flux increases because more ions have had a longer distance to accelerate to the virtual detector. At 1.1 R_M, the flux (cm^{-2} s^{-1}) in Case A peaks at 1.7×10^5 between 1 and 3 eV and the energy limit extends up to 50 eV. The flux in Case B peaks at 2.4×10^5 between 1 and 3 eV but the energy limit of the flux extends just above 1 keV. Note that the particle initialization includes a 2 eV offset. The peaks at this energy, especially seen near the planet, are due to this initial condition factor and would shift in energy if another value were used. As the detector observes the O^+ ions further from the planet at 2.5 R_M, the peak fluxes for both Cases A and B shift toward 7 and 12 eV, respectively and both now peak at 7.3×10^5. However, the difference in the energy-flux signatures is most apparent at 2.5 R_M because the upper energy limit in Case A remains at 50 eV, while in Case B, it extends above 10 keV. This extended upper energy limit indicates that ions produced in the corona have been accelerated and transported downtail. Additionally, the total observed fluxes for Cases A and B at 2.5 R_M are 3.6×10^6 and 7.0×10^6 cm^{-2} s^{-1}, respectively, indicating that the corona roughly doubles the observed flux.

[17] Figure 4 highlights the effect of the corona in velocity space at solar minimum for Case A (left) and Case B (right), where the detector is again located radially downtail from 1.1–2.5 R_M and integrated over an energy range of 1 eV–25 keV. Cases A and B display similar trends in particle motion: the O^+ flux is predominantly moving upward and tailward ($+Z_{MSO}$ direction), and increasing as the detector is placed further downtail. Locally produced ions, low-energy ions with fluxes below 10^5 $cm^{-2}s^{-1}sr^{-1}$, are observed closer

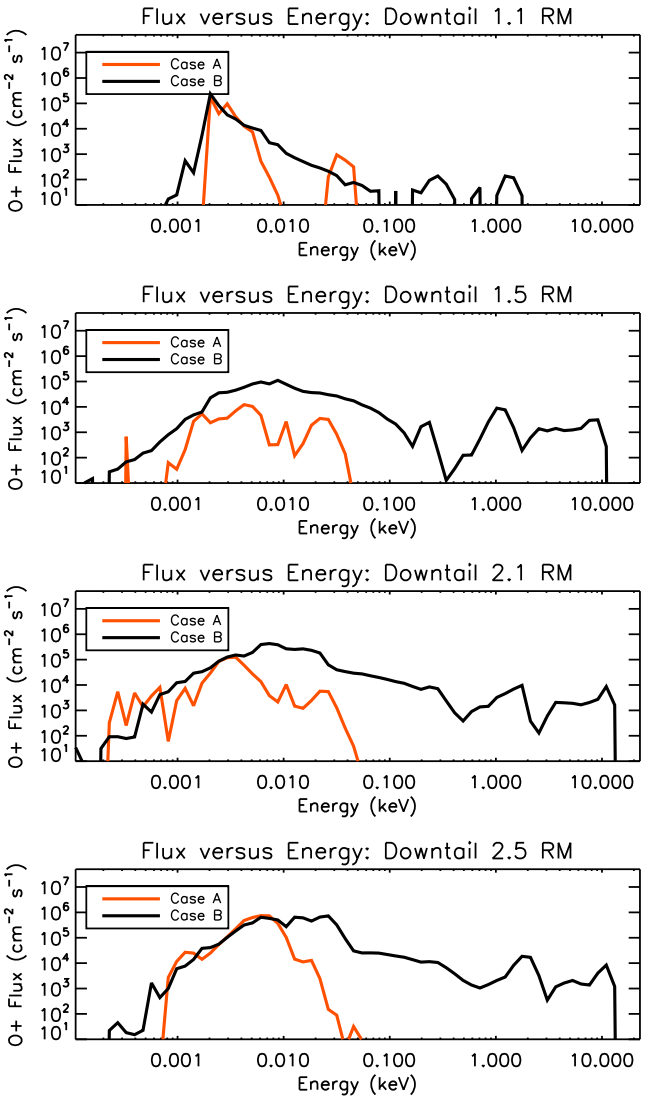

Figure 3. O^+ flux in $cm^{-2}s^{-1}$ from virtual detectors as a function of energy for Cases A and B (log scale) in red and black, respectively. Both cases are at solar minimum while only Case B includes a hot corona. The virtual detectors are positioned at 1.1–2.5 R_M downtail.

to the planet (1.1–1.5 R_M) with a broader range of flight direction angles. The range of flight direction angles, which we will refer to as flight direction coverage, is a phrase we have adopted to describe how much flux the detector observes (i.e., how much or little white space there is for a given virtual detection). At distances further downtail (2.1–2.5 R_M), the locally produced ions at 1.1–1.5 R_M have been accelerated downtail by the background convective electric field and have a more focused flight direction centered around $\phi = 180°$ and θ=90°.

[18] While the overall particle motion at the downtail detectors is similar, Cases A and B exhibit very different VSD signatures and flight direction coverage. At 1.1 R_M, the fluxes for both cases are below 10^5 $cm^{-2}s^{-1}sr^{-1}$ and moving in the upward, $+Z_{MSO}$ direction (a flight direction of θ = 0–90°). At 1.5 R_M, Case A shows much more limited flight direction coverage in comparison with Case B, indicat-

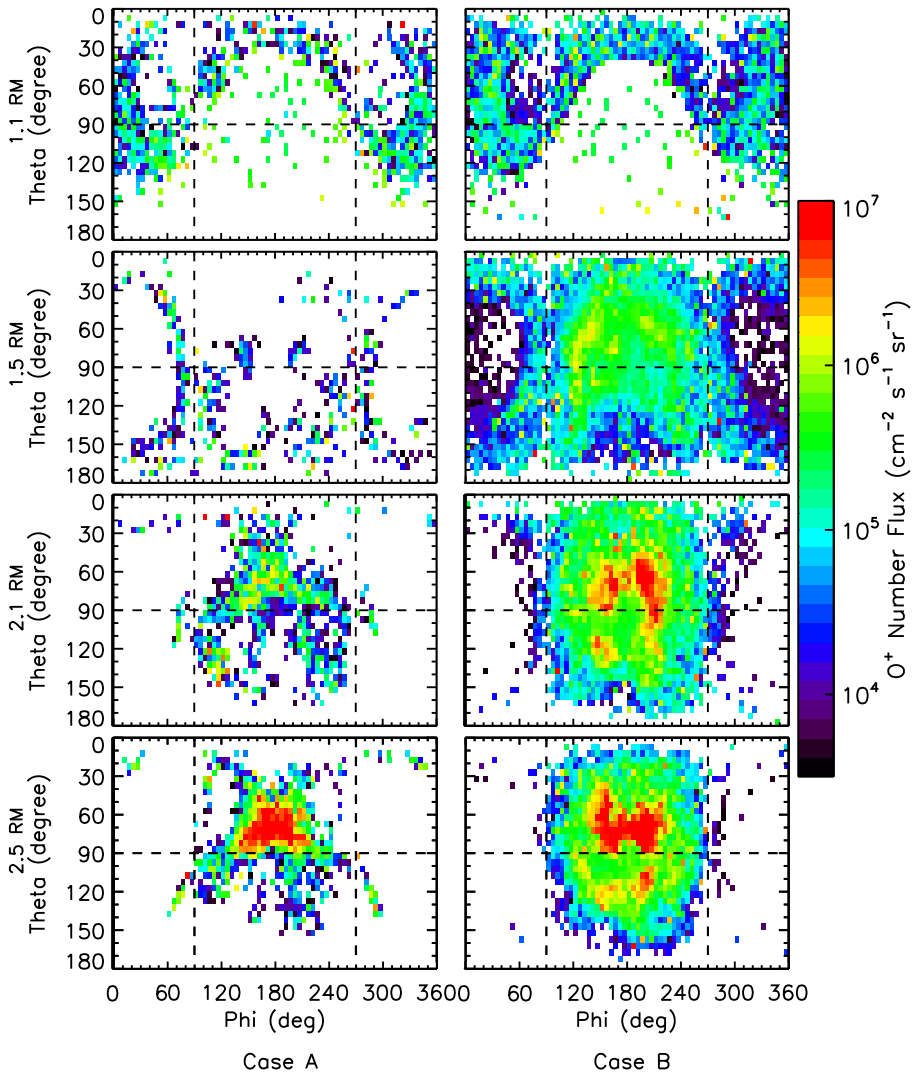

Figure 4. Velocity space distributions from several virtual detectors illustrating number flux shown with a logarithmic colorbar to the right in units of $cm^{-2}s^{-1}sr^{-1}$ for Cases A and B (left and right columns). Theta is the polar angle where $0° < \theta < 90°$ represents an upward moving flight direction and $90° < \theta < 180°$ represents a downward moving flight direction, denoted by the dashed black lines. Phi is the azimuthal angle where $90° < \phi < 270°$ represents a tailward flight direction and $0° < \phi < 90°$ and $270° < \phi < 360°$ correspond to a sunward flight direction. The virtual detector is positioned at 1.1–2.5 R_M downtail.

ing that the hot corona contributes to the majority of the flux in this region. For Case A, the flux above 10^7 $cm^{-2}s^{-1}sr^{-1}$ does not begin to accumulate and converge until 2.5 R_M downtail because without the corona, there are fewer ions to accelerate. Case B has higher ion production due to the ionized corona and consequently begins to accumulate and directionally converge above 10^7 $cm^{-2}s^{-1}sr^{-1}$ beginning at 2.1 R_M. Additionally, Case B shows high flux ion distributions with much more asymmetry. These distinct high flux populations are centered around $\phi \sim 180°$ and $\theta \sim 90°$.

3.2. Influence of the Solar Cycle

[19] By comparing Cases B and C, this section explores the solar cycle's influence on O^+ velocity distributions, particularly near the magnetic pile up boundary (MPB) and bow shock (BS) regions. This dayside region is interesting because some models and observations suggest that the EUV flux has a negligible effect on the MPB and BS location [*Vignes et al.*, 2000; *Bertucci et al.*, 2005; *Modolo et al.*, 2006; *Trotignon et al.*, 2006; *Lundin et al.*, 2007]. Consequently, the effect of the solar cycle on ion trajectories can be directly compared in identical locations on the dayside.

[20] Figure 5 compares the fluxes for Cases B and C at virtual detectors from 1.3 to 1.9 R_M radially extending from the South Pole. Cases B (solar minimum) and C (solar maximum) have similar signatures in flux versus energy, but Case B clearly shows fluxes roughly an order of magnitude below those of Case C. At 1.3 R_M, the total observed flux for Cases B and C are 1.4×10^6 and $3.6 \times 10^7 cm^{-2}s^{-1}$, respectively. It should be noted that the total flux and the upper energy limit are higher at 1.3 R_M than at 1.9 R_M as opposed to the downtail case (Figure 3) where the flux increased with distance from the planet. As *Curry et al.* [2013] discussed, the convective electric field has a $+Z_{MSO}$ component, so particles in

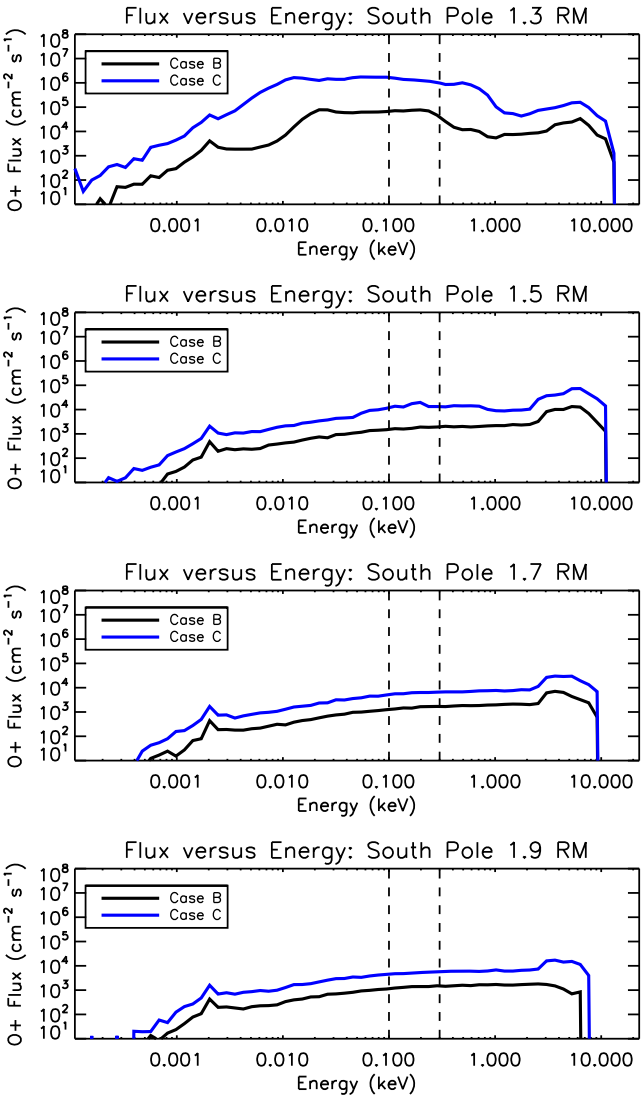

Figure 5. O^+ flux in $cm^{-2}s^{-1}$ from virtual detectors as a function of energy for Cases A and B (log scale) in red and black, respectively. Both cases include a corona where Case B is at solar minimum and Case C is at solar maximum. The virtual detectors are positioned at 1.3–1.9 R_M radially over the South Pole.

the southern hemisphere near the MPB travel upward toward the planet. Thus, particles produced at 2.5 R_M are accelerated for longer distances to the virtual detector at 1.3 R_M and thus have higher energies (the path length dl is larger when integrating $E \cdot dl$). The final difference in the energy-flux signatures is the slight peak at 1.5 R_M in Case C that does not exist for Case B (highlighted by the dashed black lines between 100 and 300 eV), a feature which will be expanded on later.

[21] Figure 6 highlights the effect of the solar cycle by comparing the velocity space for Cases B and C at 1.3–1.9 R_M over the southern pole. The virtual detectors are placed directly beneath the planet and reflect velocity space for a specific IMF configuration (a Parker spiral in the away sector) with the flux integrated from 1 eV to 25 keV. From 1.9–1.5 R_M, both Cases B and C exhibit a high flux source moving upward and tailward centered at θ =∼30° and ϕ =∼180° (+Z_{MSO}, –X_{MSO} components). As seen in Figure 5, the flux increases for both cases as the detector is moved closer to the planet and at 1.3 R_M, the high flux source broadens with more flight direction coverage as more particles are accelerated up to the detector. While Cases B and C have an extraordinarily similar flux versus energy signature in Figure 5, now that subtle increase in the flux near ∼200 eV at 1.5 R_M can be seen in velocity space. Case C clearly depicts two additional high flux beams at 1.5 R_M moving downward toward dawn and dusk at ϕ =∼90°, 270° and θ =∼170° (±Y_{MSO}, –Z_{MSO} directional components), which correspond to the small peak in flux versus energy at 200 eV. As Figures 7–9 will show, this velocity space signature is a result of the solar cycle's influence on the field line configuration that dictates the O^+ gyroradius.

[22] First, we demonstrate this by analyzing the origin of these downward moving particles hitting the detector at 1.5 R_M. Figure 7 illustrates the origin (marked in rectangular cells) of any particle that was observed at 1.5 R_M with a downward flight direction of $\theta \geq 90°$. In MSO Cartesian coordinates, the four panels correspond to the *XY*, *YZ*, *XZ*, and 3-D view of the cell origins. Red cells represent Case B while blue cells represent Case C. Figure 7 illustrates that Case C produced ions from across the dayside sector (inside the MPB) and down throughout the South Pole while Case B only produced ions in the local vicinity surrounding the detector at 1.5 R_M.

[23] Next, we need to understand why particles originating from the subsolar region were able to reach the detector in Case C while not in Case B. Figure 8 illustrates particles that were launched from one of the origin cells, located at 1.26 R_M and λ = –20° below the subsolar point, and traced throughout the simulation. Figure 8 uses the same color scheme where red cells represent Case B and blue cells represent Case C. The top panel is a close view of the particle trajectories, where the asterisks denote the beginning of their flight path and the circles denote the end of their flight path. The particles in Case B begin to gyrate and soon hit the inner boundary of 300 km, representing precipitation back into the atmosphere. While some of the particles in Case C have a similar fate, the particles have a tighter gyroradius and mostly continue gyrating and accelerating under the planet. The bottom panel is a full view of the simulation to illustrate the entire trajectory of the escaping particles in Case C. These particles gyrate under the planet, hit the detector at 1.5 R_M and then continue being swept tailward until they reach the outer boundary of 3 R_M. Because the O^+ ions are moving from the subsolar region downwards under the South Pole, the VSD signatures reflect the two beams with a downward flight direction of $\theta \geq 90°$. Due to the larger gyroradius for Case B, particles originating near the subsolar region precipitate back into the atmosphere and do not reach the detector at 1.5 R_M.

[24] This is an important point because the solar wind conditions were the same for Cases B and C and only the neutral atmosphere (see Figure 1) and EUV flux changed. Because the MTP simulation is not self-consistent, the background MHD fields must be static. So for the gyroradius to change in the same location, the field lines must be different for the two cases. Figure 9 illustrates the conditions that drive this particular velocity space signature for cells at 1.26 R_M and

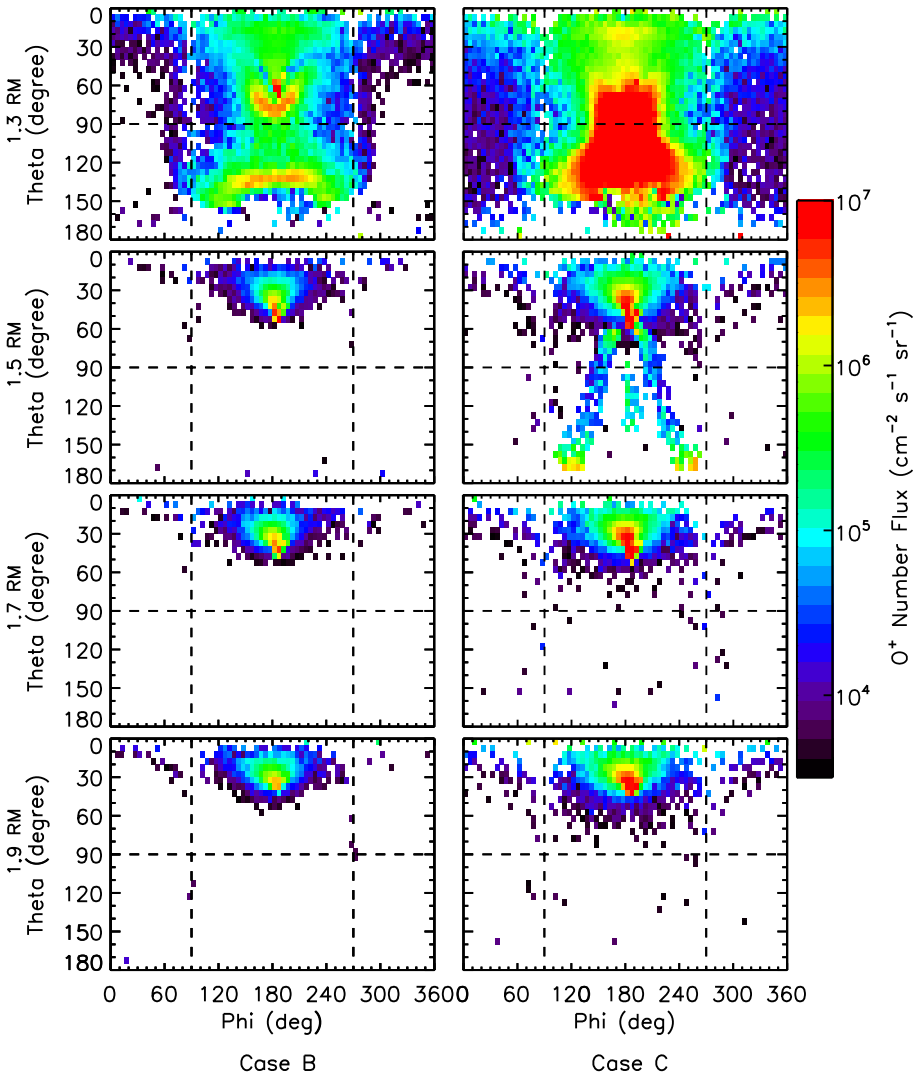

Figure 6. Velocity space distributions from several virtual detectors illustrating number flux shown with a logarithmic colorbar to the right in units of $cm^{-2}s^{-1}sr^{-1}$ for Cases B–C (left and right columns). Theta is the polar angle where $0° < \theta < 90°$ represents an upward moving flight direction and $90° < \theta < 180°$ represents a downward moving flight direction, denoted by the dashed black lines. Phi is the azimuthal angle where $90° < \phi < 270°$ represents a tailward flight direction and $0° < \phi < 90°$ and $270° < \phi < 360°$ correspond to a sunward flight direction. The virtual detector is positioned at 1.3–1.9 R_M in the southern pole.

latitude $\lambda = –20°$, plotted over local time. The magnitude of the magnetic fields are on the left axis and plotted in the solid black and blue lines for Cases B and C, respectively. The gyroradius, defined here with the particle velocity set to the pickup drift speed of the local E/B ratio, is plotted against the right axis in dashed black and blue lines for Cases B and C.

[25] Clearly, the magnetic field in Figure 9 is larger for Case C, which contributes to a smaller O^+ gyroradius. The magnetic field is larger during solar maximum because the ion production is greater and subsequently more ions mass load the solar wind. This mass loading then causes the ionospheric and solar wind thermal pressure to increase [*Ma et al.*, 2004], which subsequently drives up the magnetic field pressure and strength and causes the ions to have a smaller gyroradius. Again, this result is for an away sector Parker spiral IMF configuration (excluding crustal fields) and this IMF gives rise to the particular asymmetries in the magnetic field at this local time and latitude.

[26] In summary, the solar maximum case both increases the flux through a given detector and has a distinct signature in velocity space. When examining the South Pole detector at 1.5 R_M, the 200 eV peak in Figure 5 corresponded to the beams of downward moving flux in velocity space in Figure 6. Then Figure 7 offered a visual representation of the origin of these ions with downward flight directions ($–Z_{MSO}$ or $\theta \geq 90°$) hitting the detector at 1.5 R_M. Figure 8 illustrated O^+ ions launched from one of these cells of origin and traced throughout the simulation, revealing that the ions in the solar minimum case had such large gyroradii that they would always precipitate back into the atmosphere. Recall that the MTP simulation launches the same number of particles per cell and the only difference is the enhanced O^+

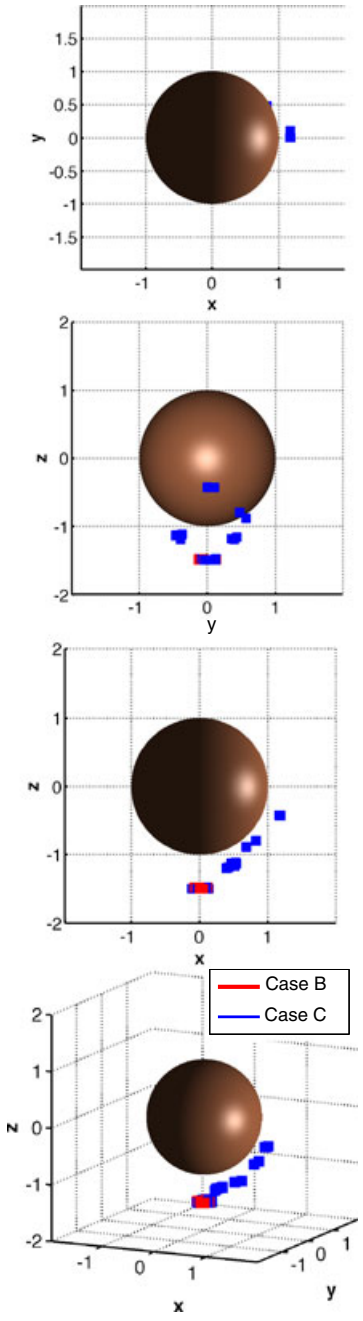

Figure 7. The four panels correspond to the *XY*, *YZ*, *XZ*, and 3-D view of the cell origins in MSO coordinates. Red cells represent Case B while blue cells represent Case C. The sun is in the $+X$ sector.

production during solar maximum. If the ion density were the only parameter changed, it would only affect the weighting of the particles and the solar minimum Case B would have the same velocity space signature but with less flux. This means that the electric and magnetic fields were different between the solar minimum and maximum cases due to mass loading of the solar wind, as seen in Figure 9. So the solar maximum case manifested itself in the velocity space because the particles near a stronger magnetic field gyrated more tightly around the field line and were transported under the planet and downtail. The particles in a weaker magnetic field (solar minimum Case B) had a larger gyroradius on the dayside and encountered the upper atmosphere, or for this simulation, crossed the inner boundary of 300 km.

3.3. Ion Escape

[27] The final point of comparison in examining the effect of the corona and solar cycle is the O^+ escape. While the simulation did not include the crustal magnetic fields, these idealized cases isolate the conditions affecting escape and are a useful comparison for other unmagnetized bodies. Again, it should be noted that the results are for specific IMF conditions (an away sector Parker spiral for this simulation) and represent the behavior of high altitude ions ($\geq$ 300 km).

[28] Figure 10 illustrates the spatial distribution of O^+ loss (s^{-1}) on a 3 R_M shell for Cases A, B, and C (top, middle, and bottom panels, respectively). The axes are in local time (hours) and latitude (°), where midnight at $\lambda = 0°$ corresponds to the downtail point at 3 R_M along the $-X_{MSO}$ line, and $\lambda = +90°$ at any local time corresponds to the North

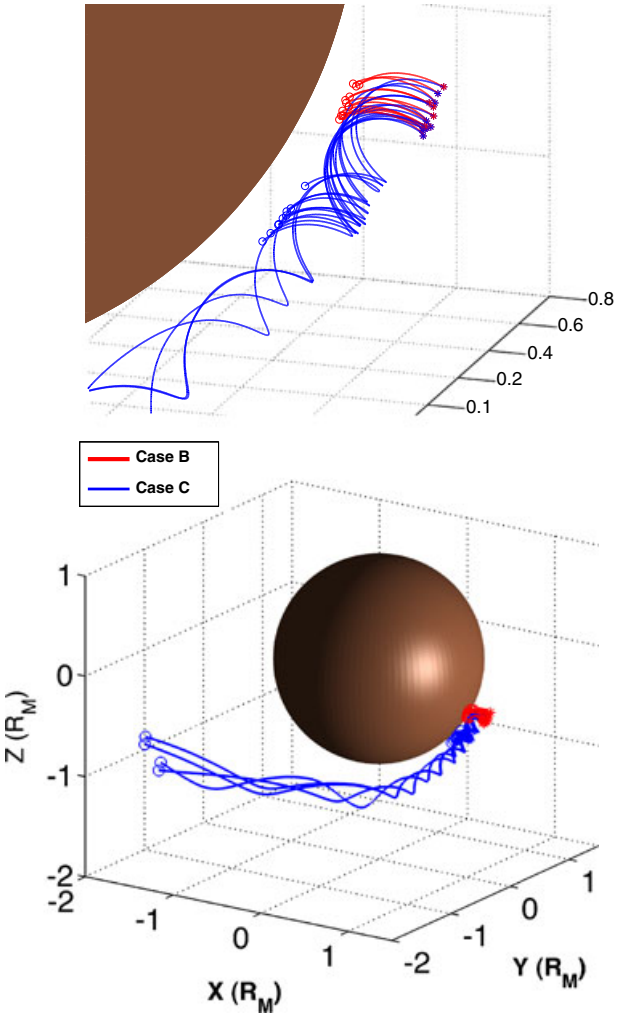

Figure 8. Particle traces launched from 1.26 R_M and 20° below the subsolar point. Case B is in red while Case C is in blue; asterisks denote the beginning of the particle trajectory and circles denote the end of the trajectory. The top panel is a zoomed view of the particle trace and the bottom panel illustrates the trajectories in the full simulation space.

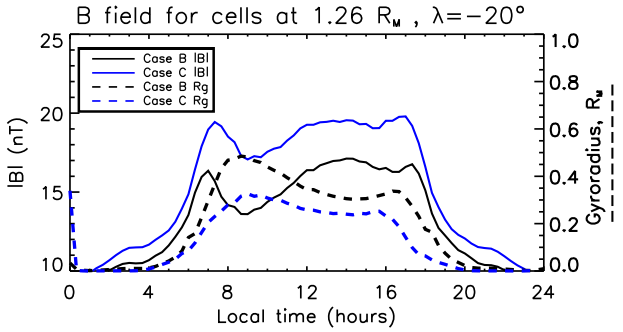

Figure 9. The magnetic fields and the gyroradius for solar minimum Case B (black lines) and solar maximum Case C (blue lines). The left *y* axis measures the magnetic field in nT (solid lines) and the right *y* axis measures the gyroradius in R_M (dashed lines). The values are plotted in local time at $\lambda = -20°$.

Pole. Beginning with Case A, the loss is concentrated in the northern pole and downtail region, with very little O^+ loss in the southern hemisphere (at latitudes $\lambda \leq 0°$). Cases B and C exhibit more loss due to the ionized corona, with loss well above 10^{18} s^{-1} throughout the southern hemisphere, denoted by the black contour lines. Case C has the highest loss rate, focused directly downtail but with enhanced loss in the northern pole. All three cases exhibit asymmetric loss in the northern polar dawn region (local time ~8–12 h and λ = 60–90°). This asymmetry in O^+ loss at Mars has also been observed by *Dubinin et al.* [2006] and modeled by *Fang et al.* [2008], *Kallio and Jarvinen* [2012], and *Curry et al.* [2013].

[29] In order to directly quantify and compare the O^+ escape in each case, Figure 11 illustrates the escape percentage at each 5° latitude ring on the 3 R_M shell. This percentage is the ratio of the escape at each latitude to the total escape on the 3 R_M shell for that case (see the bottom panel highlighting a given latitude). In Case A (red line), the escape from the northern pole region dominates with almost 20% of the O^+ escaping at $\lambda = +75°$. In case B (black line), the loss profile shifts and the polar and tailward loss are comparable at 13% escaping with $\lambda = +75°$ and 10% escaping at $\lambda = 0°$. Finally, in Case C (blue line), the increase to solar maximum clearly shifts the dominant escape to the tailward region with over 20% of the O^+ escaping at $\lambda = 0–5°$. Thus, the inclusion of the corona and the solar cycle contribute to the tailward and southern hemisphere escape.

[30] Table 1 compares the loss rates for each case on the spherical shell at 3 R_M. Each case is listed with the following parameters: the solar cycle, the inclusion of the corona, the rate (s^{-1}) of ion precipitation into the atmosphere at the lower boundary (inner loss), the rate (s^{-1}) of ion escape through the outer boundary (outer loss), and the efficiency, which is the ratio of the outer loss to the total production of O^+ ions (corresponding to inner + outer losses). This last parameter is particularly telling because the efficiency indicates the likelihood that particles will escape from the simulation domain.

[31] Beginning with Case A, the outer loss is roughly half of the rate for the inner loss, which contributes to only 32.3% of the produced particles escaping. This result is physically intuitive in that the lack of high altitude O^+ ion production results in a smaller fraction of the produced O^+ escaping. Case B, which includes the corona for solar minimum, results in the inner and outer loss rates being comparable and 47.8% of the ions escaping. This is the highest efficiency among all three cases because the corona contributes to the production of high altitude ions, which are then accelerated out of the simulation domain. While Case C might be expected to have the highest efficiency due to having the highest O^+ escape, the efficiency is marginally lower. This is because the solar maximum conditions drive more ion production at lower altitudes in the denser neutral atmosphere. Subsequently, Case C has a higher rate of inner loss that leads to a slightly lower efficiency at 45.7%.

[32] The escape rates from Table 1 are higher but in general agreement with both models and observations and will be discussed further in the context of the community-wide model comparison [*Brain et al.*, 2012]. It has been found that the *inclusion* of the crustal magnetic field in fact lowers the escape rate because it acts as a shield against solar

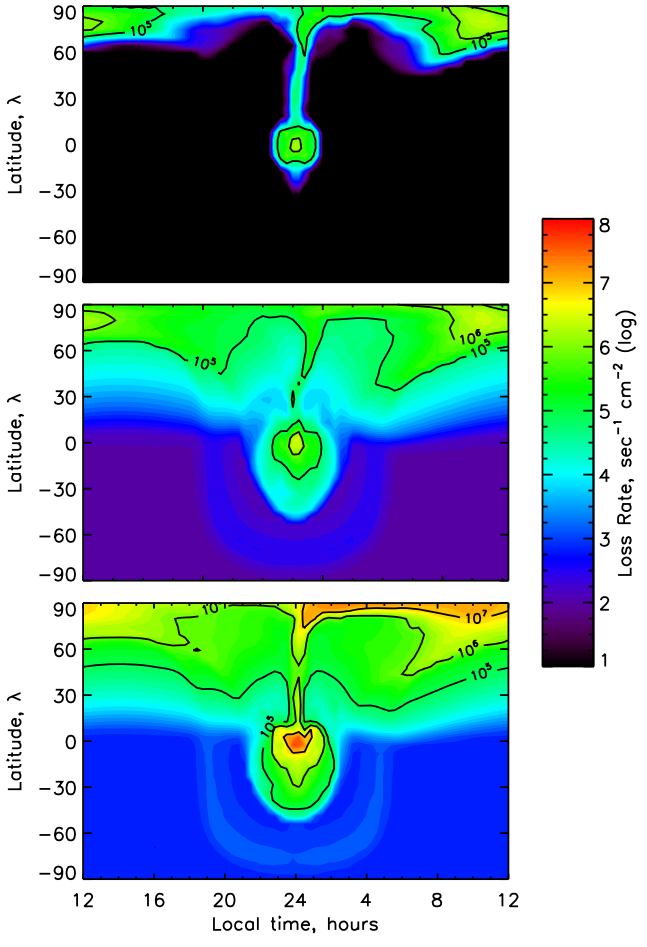

Figure 10. Contour plots of the O^+ loss for Case A (top), Case B (middle), and Case C(bottom). The *x* axis is local time in hours and the *y* axis is the latitude, in °, on a 3 R_M shell; a latitude of $\lambda = +90°$ corresponds to the North Pole and $\lambda = -90°$ corresponds to the southern pole. The colorbar is logarithmic loss in cm^{-2} sec^{-1} from 10^1–10^8 and are overlays for various flux levels, labeled accordingly from 10^4–10^6 cm^{-2} sec^{-1}.

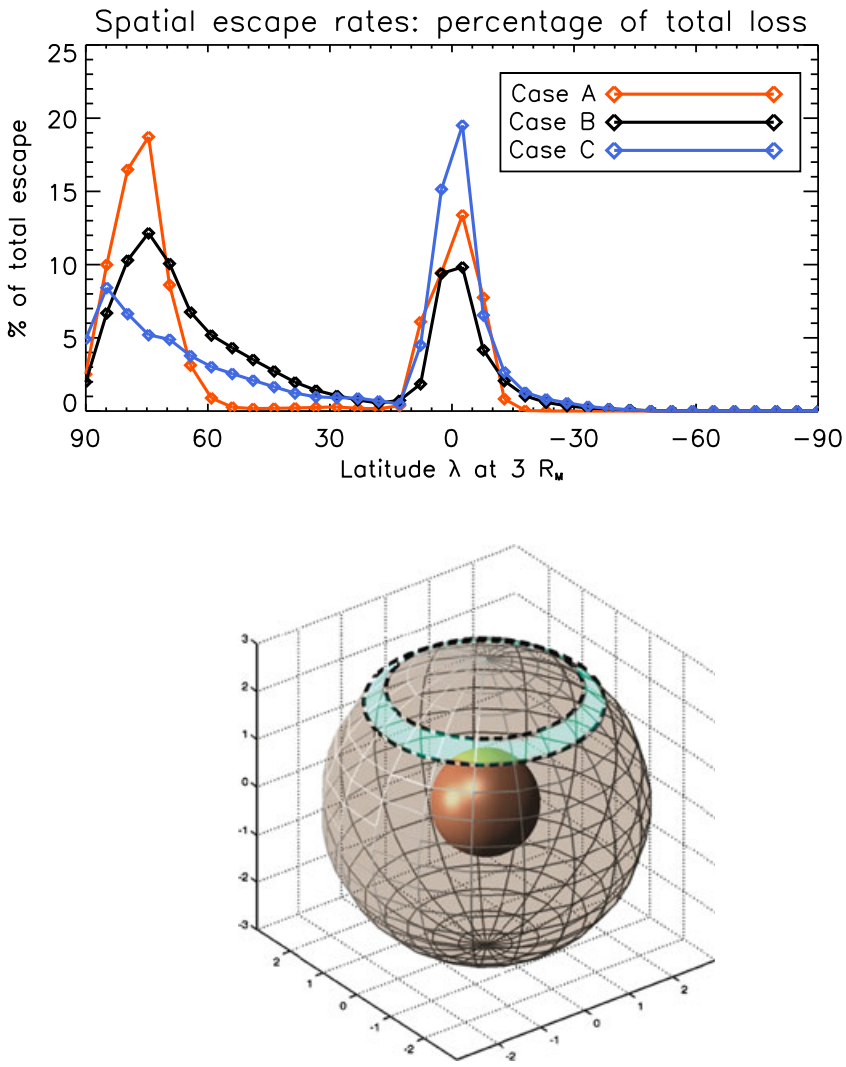

Figure 11. The escape is calculated at each latitude, in °, on a 3 R_M shell; a latitude of 90° corresponds to the North Pole, 0° corresponds to the equator and –90° corresponds to the southern pole. The loss at each latitude is a percentage of the total loss. The bottom panel illustrates a latitude band over which the loss is integrated on the 3 R_M shell.

wind erosion [*Fraenz et al.*, 2006; *Fang et al.*, 2010; *Dubinin et al.*, 2011; *Lundin et al.*, 2011b], and subsequently the escape rates presented in this study are substantially higher than escape rates calculated in the presence of a magnetic field. For this reason, it is especially useful to compare our escape rates with rates from other studies that also exclude Mars' crustal magnetic fields. *Terada et al.* [2009] used an MHD model and found O^+ escape rates of 9.5×10^{23} s^{-1} during solar minimum. *Modolo et al.* [2005] used a hybrid model, which included a hot oxygen corona, and found rates of 5.2×10^{23} and 2.4×10^{24} O^+ s^{-1} for solar minimum and maximum, respectively (an increased ratio of 4.6). *Brecht and Ledvina* [2010] also used a hybrid model and calculated the O^+ loss (s^{-1}) at solar minimum to be 8.0×10^{24} and 5.2×10^{25} at solar maximum (an increased ratio of 6.5). The ratio of O^+ loss from solar maximum to minimum in our study is 8.4.

4. Summary

[33] As discussed in sections 2.2 and 3, the corona and solar cycle have unique influences on the production, acceleration, and escape of O^+. The three cases presented for comparison were: Case A using solar minimum conditions without a corona, Case B using solar minimum conditions

Table 1. O^+ Loss Rates (#s^{-1}) and Ratios

Case	Cycle	Corona	Inner Loss	Outer Loss	Efficiency
Case A	Min	No	6.56×10^{23}	3.13×10^{23}	32.3%
Case B	Min	Yes	8.04×10^{23}	7.36×10^{23}	47.8%
Case C	Max	Yes	7.32×10^{24}	6.17×10^{24}	45.7%

with a corona, and Case C using solar maximum conditions with a corona.

[34] Beginning with the neutral atmosphere in section 2.2, Figure 1 highlights the different neutral profiles of atomic oxygen. The O^+ ionization rates vary as a function of this neutral profile and solar cycle, as seen in Figure 2. Because the O^+ escape is a subject of disagreement, the O^+ production is important to consider.

[35] Section 3 quantifies the effect of the corona and solar cycle using virtual detectors to construct velocity space distributions and spatial escape maps. As discussed in section 3.1, the inclusion of a hot corona dramatically increases the high energy flux downtail. Examining a series of virtual detectors downtail, Figure 3 shows that Case A has very little O^+ flux above 50 eV and much less flight direction coverage than Case B, whose upper energy limit extends above 10 keV and has much higher flight direction coverage. The downtail observed fluxes at 2.5 R_M are 3.6 and 7.0 $\times$ 10^6 cm^{-2} sec^{-1} for Cases A and B, respectively, which suggests that the inclusion of a corona almost doubles the flux accelerated downtail.

[36] Section 3.2 discusses the influence of the solar cycle on the observed O^+ flux and ion trajectories. At the South Pole, as the detector approaches the planet, it observes high energy, accelerated ions from the ionized corona. The flux observed at the southern pole is roughly an order of magnitude higher at solar maximum than at solar minimum, as seen in Figure 5. Additionally, some of this flux comes down from the dayside subsolar region at solar maximum, as illustrated in Figures 6–9. These downward moving beams of ions originate from inside of the bow shock near the subsolar point, $\sim$1.2–1.4 R_M, and at lower latitudes ($\sim$0 through –90°). During solar maximum, the increased mass loading of the solar wind causes the magnetic pressure and field strength to increase on the dayside, which in turn decreases the ion gyroradius and allows particles to be accelerated underneath the planet and downtail. At solar minimum, the solar wind is still mass loaded, but much less so which results in a weaker magnetic field and much larger gyroradii; ions thus cannot avoid precipitating into the planetary neutral atmosphere.

[37] Finally, section 3.3 addresses the influence of the corona and solar cycle on the overall O^+ escape. As with the case of the total flux, the inclusion of the hot corona roughly doubles the outer escape on a 3 R_M shell during solar minimum, and the solar maximum condition increases the escape almost an order of magnitude. In addition to an increase in O^+ loss, there is an increase in the efficiency of Cases B and C, indicating that the likelihood of each ion produced is more likely to escape with the inclusion of the hot oxygen corona.

[38] These results are part of a community-wide model comparison in order to quantify the role of the solar cycle and corona with respect to the transport and escape of O^+. A particular niche of a test particle simulation includes high resolution VSDs, which the MTP constructed from 1.5 billion test particles following background electric and magnetic fields. The inclusion of a hot neutral corona greatly affects the high altitude O^+ production and subsequent acceleration to energies above 10 keV. The solar cycle contributes to an order of magnitude increase in O^+ escape between the solar minimum and maximum cases.

[39] **Acknowledgments.** This work was funded by the NASA Goddard Space Flight Center under the Graduate Student Research Program. We also acknowledge support for the University of Michigan work from the NASA grants NNX10AL84H and NNX11D80G as well as the NSF grant AST-0908311 and for the University of Colorado work with NSF grant AST-0908472. The authors would also like to thank Elizabeth Hildinger for her valuable expertise in technical writing.

[40] Masaki Fujimoto thanks the reviewer for their assistance in evaluating this paper.

References

Andersson, L., R. E. Ergun, and A. I. F. Stewart (2010), The combined atmospheric photochemistry and ion tracing code: Reproducing the viking lander results and initial outflow results, *Icarus*, *206*(1), 120–129, doi:10.1016/j.icarus.2009.07.009.

Barabash, S., and M. Holmstrom (2002), Energetic neutral atoms at Mars 4. Imaging of planetary oxygen, *J. Geophys. Res.*, *107*(A10), 1280, doi:10.1029/2001JA000326.

Bauske, R., A. Nagy, T. Gombosi, D. De Zeeuw, K. Powell, and J. Luhmann (1998), A three-dimensional MHD study of solar wind mass loading processes at Venus: Effects of photoionization, electron impact ionization, and charge exchange, *J. Geophys. Res.*, *103*(A10), 625–638.

Bertucci, C., C. Mazelle, and M. Acuna (2005), Structure and variability of the martian magnetic pileup boundary and bow shock from MGS MAG/ER observations, *Adv. Space Res.*, *36*(11), 2066–2076, doi:10.1016/j.asr.2005.05.096.

Boesswetter, A., et al. (2007), Comparison of plasma data from ASPERA-3/Mars-Express with a 3-D hybrid simulation, *Ann. Geophys.*, *25*, 1851–1864.

Bougher, S. W., S. Engel, D. Hinson, and J. Murphy (2004), MGS radio science electron density profiles: Interannual variability and implications for the martian neutral atmosphere, *J. Geophys. Res.*, *109*, E03010, doi:10.1029/2003JE002154.

Bougher, S. W., P. Blelly, M. Combi, J. L. Fox, I. Mueller-Wodarg, A. Ridley, and R. Roble (2008), Neutral upper atmosphere and ionosphere modeling, *Space Sci. Rev.*, *139*, 107–141.

Brain, D., et al. (2010), A comparison of global models for the solar wind interaction with Mars, *Icarus*, *206*(1), 139–151, doi:10.1016/j.icarus.2009.06.030.

Brain, D., et al. (2012), Comparison of global models for the escape of martian atmospheric plasma, Abstract P13C-1969 presented at 2012 Fall Meeting, San Francisco, Calif., 3–7 Dec. 2012, http://fallmeeting.agu.org/2012/eposters/eposter/p13c-1969/.

Brecht, S. H., and S. A. Ledvina (2010), The loss of water from Mars: Numerical results and challenges, *Icarus*, *206*(1), 164–173, doi:10.1016/j.icarus.2009.04.028.

Chaufray, J. Y., R. Modolo, F. Leblanc, G. Chanteur, R. E. Johnson, and J. G. Luhmann (2007), Mars solar wind interaction: Formation of the martian corona and atmospheric loss to space, *J. Geophys. Res.*, *112*, E09009, doi:10.1029/2007JE002915.

Cipriani, F., F. Leblanc, and J. J. Berthelier (2007), Martian corona: Nonthermal sources of hot heavy species, *J. Geophys. Res.*, *112*, E07001, doi:10.1029/2006JE002818.

Cravens, T. E., J. U. Kozyra, A. Nagy, T. Gombosi, and M. Kurtz (1987), Electron impact ionization in the vicinity of comets, *J. Geophys. Res.*, *92*, 7341–7353.

Curry, S. M., M. W. Liemohn, X. Fang, Y. J. Ma, and J. R. Espley (2013), The influence of production mechanisms on pick-up ion loss at Mars, *J. Geophys. Res.*, *118*, 554–569, doi:10.1029/2012ja017665.

Dubinin, E., M. Fraenz, J. Woch, E. Roussos, S. Barabash, R. Lundin, J. D. Winningham, R. A. Frahm, and M. Acuna (2006), Plasma morphology at Mars. Aspera-3 observations, *Space Sci. Rev.*, *126*(1–4), 209–238, doi:10.1007/s11214-006-9039-4.

Dubinin, E., M. Fraenz, A. Fedorov, R. Lundin, N. Edberg, F. Duru, and O. Vaisberg (2011), Ion energization and escape on Mars and Venus, *Space Sci. Rev.*, *162*(1–4), 173–211, doi:10.1007/s11214-011-9831-7.

Fang, X., M. W. Liemohn, A. F. Nagy, Y. Ma, D. L. De Zeeuw, J. U. Kozyra, and T. H. Zurbuchen (2008), Pickup oxygen ion velocity space and spatial distribution around Mars, *J. Geophys. Res.*, *113*, A02210, doi:10.1029/2007JA012736.

Fang, X., M. W. Liemohn, A. F. Nagy, J. G. Luhmann, and Y. Ma (2010), On the effect of the martian crustal magnetic field on atmospheric erosion, *Icarus*, *206*(1), 130–138, doi:10.1016/j.icarus.2009.01.012.

Fox, J. L. (2009), Morphology of the dayside ionosphere of mars: Implications for ion outflows, *J. Geophys. Res.*, *114*, E12005, doi:10.1029/2009je003432.

Fox, J. L., and A. Hac (1997), Spectrum of hot O at the exobases of the terrestrial planets, *J. Geophys. Res.*, *102*(A11), 24,005–24,011, doi:10.1029/97JA02089.

Fraenz, M., et al. (2006), Plasma intrusion above Mars crustal fields: Mars Express ASPERA-3 observations, *Icarus*, *182*(2), 406–412, doi:10.1016/j.icarus.2005.11.016.

Harnett, E. M., and R. M. Winglee (2006), Three-dimensional multi-fluid simulations of ionospheric loss at mars from nominal solar wind conditions to magnetic cloud events, *J. Geophys. Res.*, *111*, A09213, doi:10.1029/2006ja011724.

Jakosky, B. M., and R. J. Phillips (2002), Mars volatile and climate history, *Nature*, *412*, 237–244.

Jin, H., K. Maezawa, and T. Mukai (2006), Effects of charge exchange and electron impact ionization on the formation of the magnetic pileup boundary at Mars, *J. Geophys. Res.*, *111*, A05306, doi:10.1029/2005ja011127.

Kallio, E., and R. Jarvinen (2012), Kinetic effects on ion escape at Mars and Venus: Hybrid modeling studies, *Earth Planets Space*, *64*(2), 157–163, doi:10.5047/eps.2011.08.014.

Kallio, E., K. Liu, R. Jarvinen, V. Pohjola, and P. Janhunen (2010), Oxygen ion escape at Mars in a hybrid model: High energy and low energy ions, *Icarus*, *206*(1), 152–163, doi:10.1016/j.icarus.2009.05.015.

Kallio, E., J.-Y. Chaufray, R. Modolo, D. Snowden, and R. Winglee (2011), Modeling of Venus, Mars, and Titan, *Space Sci. Rev.*, *162*(1–4), 267–307, doi:10.1007/s11214-011-9814-8.

Liu, Y., A. Nagy, C. Groth, D. De Zeeuw, T. Gombosi, and K. Powell (1999), 3D multifluid MHD studies of the solar wind interaction with Mars, *Geophys. Res. Lett.*, *26*(17), 2689–2692.

Luhmann, J. G., and J. U. Kozyra (1991), Dayside pickup oxygen ion precipitation at Venus and Mars spatial distributions energy deposition and consequences, *J. Geophys. Res.*, *96*, 5457–5467.

Lundin, R., H. Lammer, and I. Ribas (2007), Planetary magnetic fields and solar forcing: Implications for atmospheric evolution, *Space Sci. Rev.*, *129*(1–3), 245–278, doi:10.1007/s11214-007-9176-4.

Lundin, R., S. Barabash, E. Dubinin, D. Winningham, and M. Yamauchi (2011a), Low-altitude acceleration of ionospheric ions at Mars, *Geophys. Res. Lett.*, *38*, L08108, doi:10.1029/2011GL047064.

Lundin, R., S. Barabash, M. Yamauchi, H. Nilsson, and D. Brain (2011b), On the relation between plasma escape and the martian crustal magnetic field, *Geophys. Res. Lett.*, *38*, L02102, doi:10.1029/2010GL046019.

Ma, Y., A. Nagy, I. V. Sokolov, and K. C. Hansen (2004), Three-dimensional, multispecies, high spatial resolution MHD studies of the solar wind interaction with Mars, *J. Geophys. Res.*, *109*, A07211, doi:10.1029/2003JA010367.

Modolo, R., G. Chanteur, E. Dubinin, and A. Matthews (2005), Influence of the solar EUV flux on the martian plasma environment, *Ann. Geophys.*, *23*, 433–444.

Modolo, R., G. Chanteur, E. Dubinin, and A. Matthews (2006), Simulated solar wind plasma interaction with the martian exosphere: Influence of the solar EUV flux on the bow shock and the magnetic pile-up boundary, *Ann. Geophys.*, *24*, 3403–3410.

Nagy, A., et al. (2004), The plasma environment of Mars, *Space Sci. Rev.*, *111*, 33–114.

Najib, D., A. F. Nagy, G. Tth, and Y. Ma (2011), Three-dimensional, multifluid, high spatial resolution MHD model studies of the solar wind interaction with Mars, *J. Geophys. Res.*, *116*, A05204, doi:10.1029/2010JA016272.

Shinagawa, H., and S. W. Bougher (1999), A two-dimensional MHD model of the solar wind interaction with Mars, *Earth Planets Space*, *51*, 55–60.

Terada, N., Y. N. Kulikov, H. Lammer, H. I. Lichtenegger, T. Tanaka, H. Shinagawa, and T. Zhang (2009), Atmosphere and water loss from early Mars under extreme solar wind and extreme ultraviolet conditions, *Astrobiology*, *9*(1), 55–70, doi:10.1089/ast.2008.0250.

Trotignon, J. G., C. Mazelle, C. Bertucci, and M. H. Acua (2006), Martian shock and magnetic pile-up boundary positions and shapes determined from the Phobos 2 and Mars Global Surveyor data sets, *Planet. Space Sci.*, *54*(4), 357–369, doi:10.1016/j.pss.2006.01.003.

Valeille, A., M. R. Combi, S. W. Bougher, V. Tenishev, and A. F. Nagy (2009), Three-dimensional study of Mars upper thermosphere/ionosphere and hot oxygen corona: 2. Solar cycle, seasonal variations, and evolution over history, *J. Geophys. Res.*, *114*, E11006, doi:10.1029/2009JE003389.

Valeille, A., M. Combi, V. Tenishev, S. W. Bougher, and A. Nagy (2010), A study of suprathermal oxygen atoms in Mars upper thermosphere and exosphere over the range of limiting conditions, *Icarus*, *206*, 18–27, doi:10.1016/j.icarus.2008.08.018.

Vignes, D., et al. (2000), The solar wind interaction with Mars: Locations and shapes of the bow shock and the magnetic pile-up boundary from the observations of the mag/er experiment onboard mars global surveyor, *Geophys. Res. Lett.*, *27*(1), 49–52, doi:10.1029/1999GL010703.